THE JOURNAL OF PHYSICAL CHEMISTRY Letters

Letter

pubs.acs.org/JPCL

Thickness-Dependent Photoelectrochemical Water Splitting on Ultrathin $LaFeO_3$ Films Grown on Nb:$SrTiO_3$

Kevin J. May,*[,†] David P. Fenning,*[,†] Tian Ming,[‡] Wesley T. Hong,[‡] Dongkyu Lee,[†,⊥] Kelsey A. Stoerzinger,[‡] Michael D. Biegalski,[∥,#] Alexie M. Kolpak,[†] and Yang Shao-Horn*[,†,‡,§]

[†]Department of Mechanical Engineering, [‡]Department of Materials Science and Engineering, and [§]Electrochemical Energy Laboratory, Massachusetts Institute of Technology, Cambridge, Massachusetts 02139, United States

[∥]Center for Nanophase Materials Sciences, Oak Ridge National Laboratory, Oak Ridge, Tennessee 37831, United States

Supporting Information

ABSTRACT: The performance of photoelectrodes can be modified by changing the material chemistry, geometry, and interface engineering. Specifically, nanoscale active layers can facilitate the collection of charge carriers. In heterostructure devices, the multiple material interfaces are particularly important, which at present are not well understood for oxides. Here, we report a detailed study of ultrathin (2−25 nm) $LaFeO_3$ films grown epitaxially on Nb-doped $SrTiO_3$. The films exhibit thickness-dependence with sensitivity to less than 10 nm in both the through-plane charge transfer conductivity and in the potential-dependent photoresponse. Supplementing photoelectrochemical measurements with X-ray photoelectron spectroscopy, spectroscopic ellipsometry, and electrochemical impedance spectroscopy, we construct a band model that accounts for this thickness dependence via a shifting valence-band offset at the film−substrate interface and the potential-dependent overlap of the depletion regions present at both the film−substrate and film-electrolyte interfaces. These results illustrate the utility of using active layer thickness and film−substrate interactions to tune the performance of photoelectrodes, providing insight for the design of efficient heterostructure oxide photoelectrochemical devices.

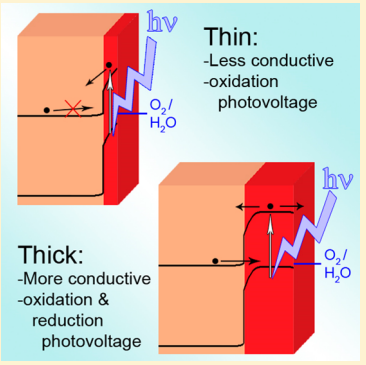

Since Fujishima and Honda's discovery of photoelectrochemical water splitting on TiO_2, there has been significant research focus on developing a stable, low-cost, and efficient photoelectrode to harness solar energy for fuel production.[1−3] Oxides such as Fe_2O_3 have the advantage of being earth-abundant, nontoxic, and chemically stable. However, most have electronic properties that are poorly suited for use in a photovoltaic or photoelectrochemical device, owing to their indirect band gaps, low charge carrier mobilities, and short minority carrier lifetimes.[4] To overcome this limitation, the axis for light absorption can be separated from the carrier collection dimension, frequently proposed in the form of nanorod electrode structures.[3−7] In addition, heterostructures offer the opportunity to divide the required device properties (e.g., absorption and long-range carrier transport) between different materials. In such architectures, and nanoscaled materials in general, control of surface and interface properties becomes critical for efficient charge transfer and ultimate device performance. Efforts are ongoing to understand the interfaces present in photoelectrochemical water splitting, including via the use of thin film model systems.[8−13] Here, we present a proof-of-concept using oxide heterostructures as a means to probe and provide insights into controlling the interfacial properties for photoelectrochemical water splitting.

We report the thickness-dependent photoelectrochemical behavior of $LaFeO_3$ thin films (2, 5, 10, and 25 nm) grown via pulsed laser deposition on Nb-doped $SrTiO_3$ (Nb:$SrTiO_3$). $LaFeO_3$ was chosen based on its band gap of ∼2.0 eV that absorbs visible-light (reported in the literature[14−16] and measured in this work, Figures S4−S5), its moderate catalytic activity for oxygen evolution,[17] and lattice-matched growth on the substrate. Although some reports of photocatalytic performance have been made for sacrificial donor-assisted water splitting and dye degradation,[16,18−22] its photoelectrochemical performance for water splitting has not yet been reported. The use of thin films provides a useful model system for examining the interactions between bulk and surface properties, which is paramount to the development of photoelectrochemical devices with nanometer-scale active layers. The effect of film thickness and applied potential on the carrier collection and charge transfer properties of the system were studied by using the films as electrodes and photoelectrodes for the oxygen evolution reaction (OER) and for fast outer-shell redox species. By characterizing the films with variable-angle spectroscopic ellipsometry, X-ray photoelectron spectroscopy, photoelectrochemical quantum efficiency, and electrochemical impedance spectroscopy, the roles of the interfaces present in the films are elucidated. The electrochemical and photoelectrochemical behavior are ex-

Received: January 24, 2015
Accepted: February 24, 2015

ACS Publications © XXXX American Chemical Society

DOI: 10.1021/acs.jpclett.5b00169
J. Phys. Chem. Lett. 2015, 6, 977−985

plained via a band model, revealing a strong dependence of the films' photoelectrode behavior on thickness.

Cyclic voltammetry revealed asymmetric current with respect to forward and reverse bias conditions in all of the $LaFeO_3$ thin films. Figure 1a shows cyclic voltammograms of $LaFeO_3$ films of different thicknesses performed in the dark at 10 mV/s in Ar-bubbled 0.1 M KOH (pH 13) with 5 mM $Fe[CN]_6^{3-}$ and 5 mM $Fe[CN]_6^{4-}$, which has an equilibrium redox potential of 1.2 V vs reversible hydrogen electrode (RHE). All the $LaFeO_3$ films had smaller reduction current (electron flow from $Nb:SrTiO_3$ substrate to $LaFeO_3$ film to electrolyte) than oxidation current (electron flow from the electrolyte to $LaFeO_3$ and then into $Nb:SrTiO_3$), with shallower slopes and less-defined reduction peaks. Because of the fast kinetics of the outer sphere $Fe[CN]_6^{4-}/Fe[CN]_6^{3-}$ redox reaction, the observed asymmetrical behavior can be attributed to rectification at the n^+-p ($Nb:SrTiO_3-LaFeO_3$) substrate–film junction ("buried" junction). Similar rectification has been seen in Sr-doped $LaFeO_3$ films and other perovskite oxides grown on $Nb:SrTiO_3$.[23−27] However, the larger oxidative current occurs at a reverse bias condition at the buried junction, indicating that the junction is highly nonideal with significant, potential-dependent reverse-bias saturation current. This nonideal rectification likely indicates the presence of a high density of interface states at the buried junction, and may be assisted by tunneling processes.[28,29]

While $LaFeO_3$ films of 5, 10, and 25 nm were found to exhibit fast oxidation kinetics of $Fe[CN]_6^{4-}$ to $Fe[CN]_6^{3-}$, the 2 nm film showed a considerable overpotential (~0.2 V shift from the equilibrium voltage) for the onset of oxidation currents. The estimated Debye length of the film, and thus the depletion width, is on the order of 1 nm (see Supporting Information). Thus, the overpotential in the 2 nm $LaFeO_3$ film may be contributed to by both an energetic barrier for transporting charge due to band alignment/bending and the subsequent depleted charge carrier (hole) density on the $LaFeO_3$ surface as a result of the n^+-p buried junction.

In contrast to the fast oxidation kinetics of $Fe[CN]_6^{4-}$ to $Fe[CN]_6^{3-}$ (Figure 1a), $LaFeO_3$ films of 5, 10, and 25 nm were found to have large overpotentials for OER (~0.4 V) and similar currents in the dark (Figure 1b). The large overpotentials can be attributed to OER kinetic losses at the film-electrolyte junction ("surface" junction).[17,30] The 2 nm film had much lower OER currents than thicker films at comparable potentials, likely owing to the significant potential required to pass current across the buried junction, as seen in Figure 1a, in addition to the OER overpotential. Illumination with a 405 nm laser led to negative voltage shifts for the onset of OER current and considerable increases in the OER current, as shown in Figure 1c. The choice of wavelength prevents any significant absorption in the substrate that could lead to photocurrent (see imaginary dielectric constants in Figure S5a-b). The $LaFeO_3$ films of 5, 10, and 25 nm show large oxidation photocurrents, despite the films being p-type (and therefore typically used for photoreduction). We attribute this result to the development of a photovoltage at the buried $Nb:SrTiO_3-LaFeO_3$ buried junction that provides additional overpotential for the OER (supported by quantum efficiency measurements below).

Increasing the thickness of $LaFeO_3$ films also results in larger reduction photocurrent at more negative potentials. This behavior is more typical of a p-type semiconductor, where minority carrier electrons can be collected at the surface for reduction. Increasing (albeit small) ORR currents as a function

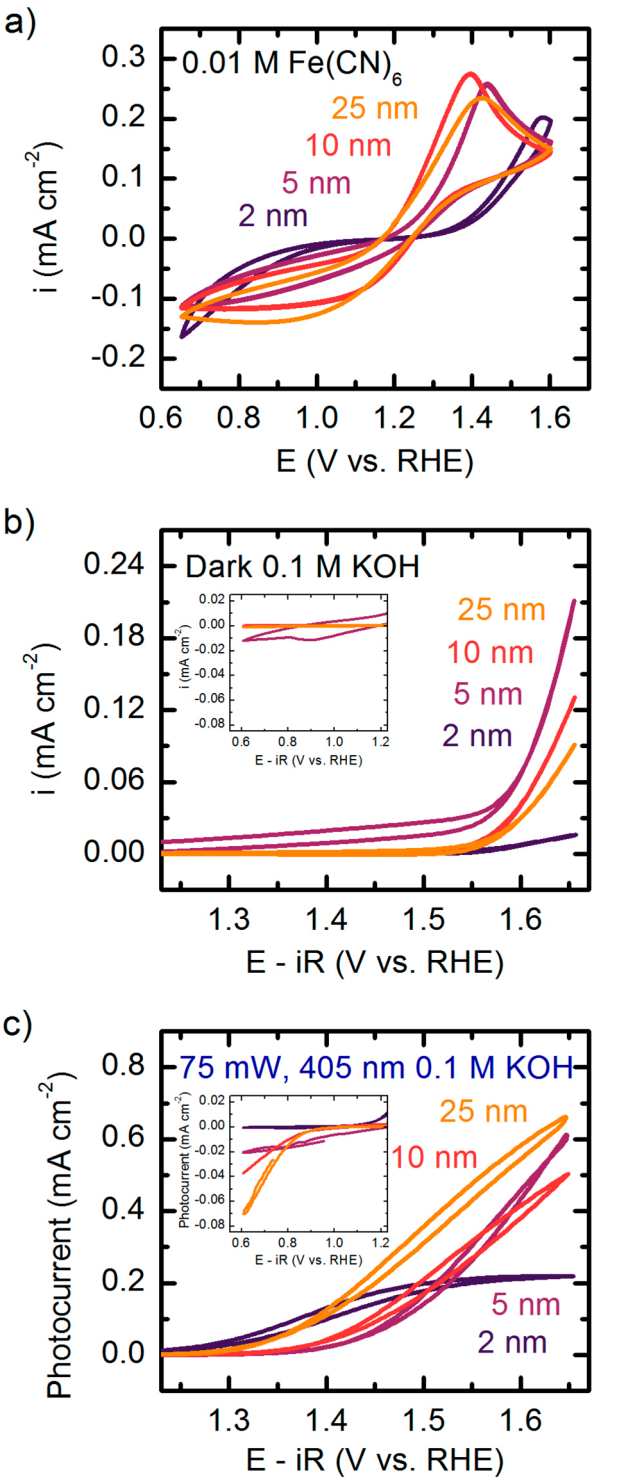

Figure 1. Cyclic voltammetry (10 mV/s) of $LaFeO_3$ thin films (thicknesses indicated), with current normalized to the film surface area of 0.25 cm^2. (a) Ar-bubbled 0.1 M KOH + 0.01 M $Fe(CN)_6$ (pH 13) the second cycle; (b) O_2-saturated 0.1 M KOH, showing the first cycle; (c) photocurrent under 405 nm laser illumination of 100 mW in O_2-saturated 0.1 M KOH, calculated as the difference between the illuminated and dark cyclic voltammograms. Insets in b and c show the ORR region of the voltammogram. It should be noted that anomalous dark current in the 5 nm film may be attributed to pinholes in the epoxy coating exposing some of the Ag paint used in the contacts, leading to Ag redox current from near 1.1 and 1.4 V RHE in the double-layer capacitive region of the voltammogram.[35]

DOI: 10.1021/acs.jpclett.5b00169
J. Phys. Chem. Lett. 2015, 6, 977−985

of thickness are seen for potentials lower than the equilibrium potentital (forward biasing of buried junction) (Figure 1c inset). The 2 nm film, on the other hand, shows only OER photoresponse, more typical of an *n*-type semiconductor and distinctly different from thicker $LaFeO_3$ films (Figure 1c).[31−34]

We have developed a semiquantitative semiconductor band model[36−41] to help explain the observed electrochemical and photoelectrochemical responses of the $LaFeO_3$ heterojunctions. The band diagrams were computed based on the experimental valence band offsets (VBOs) obtained from X-ray photoelectron spectroscopy (Figure S9), band gap from spectroscopic ellipsometry (Figures S4 and S5), along with literature values for material properties for use in a Poisson equation solver (Table S1, Supporting Information). The XPS-derived VBOs, ΔE_V, were calculated by[42]

$$\Delta E_V = (E_{CL} - E_V)^{\text{thick film}} - (E_{CL} - E_V)^{\text{bare substrate}} - (E_{CL}{}^{\text{thin film}} - E_{CL}{}^{\text{substrate}})$$

where E_{CL} and E_V are a chosen core-level energy from an element in each material (not common to both) and valence band energy, respectively. The VBO values increased with film thickness (1.98, 2.18, and 2.20 eV for the 2, 5, and 10 nm films, respectively) and at a critical thickness reaches a plateau (Figure S9d), similar to that reported for $LaCrO_3$ films grown on $SrTiO_3$.[41] The VBO in all cases is significantly larger than that expected from an Anderson-type band alignment (the electron affinity rule), frequently used for band diagrams in the literature.[43] The Anderson model alignment would result in a VBO approximately equal to the difference in the band gap between Nb:$SrTiO_3$ (3.2 eV) and $LaFeO_3$ (2.0 eV) since their electron affinities are similar (3.9 eV and 3.6−4.1 eV, respectively; see Supporting Information, Figure S11).[44,45] The experimentally determined VBO range of 1.98−2.20 eV is significantly larger than the VBO predicted from the electron affinity rule, 1.0−1.5 eV. It should be stressed that the electron affinity rule does not include effects from chemical bonding, interface dipoles, defects, and assumes a crystallographically perfect and abrupt interface; it struggles to predict alignments for materials with stronger chemical bonds and has also been critiqued on a fundamental level for being based on parameters defined by a free-surface, whereas a heterojunction is an interface between two solids.[46−48] While it is the most convenient method for estimating band offsets, more refined approaches include semiempirical modifications, tight-binding theory, and first-principles calculations such as density functional theory.[49,50] Although the experimentally determined VBO includes an assumption that the energy difference between a core level and the valence band of the film is constant (neglecting possible changes in chemical environment with film thickness), the discrepancy between the experimental VBO and the prediction from the electron affinity rule illustrates the need for accurate band alignment information when using an interface band schematic to explain experimental results.

The different band offsets as a function of thickness result in different buried junction and surface junction energetics; this will impact the current transport and photoresponse behavior of the complete substrate−film-electrolyte system. Results of the 1D Poisson-solver band diagram calculations are shown in Figure 2b for the 2 and 10 nm films, at buried junction bias conditions corresponding to 1.6 V RHE. For example, the apparent "*n*-type" photoresponse of the 2 nm $LaFeO_3$ film can

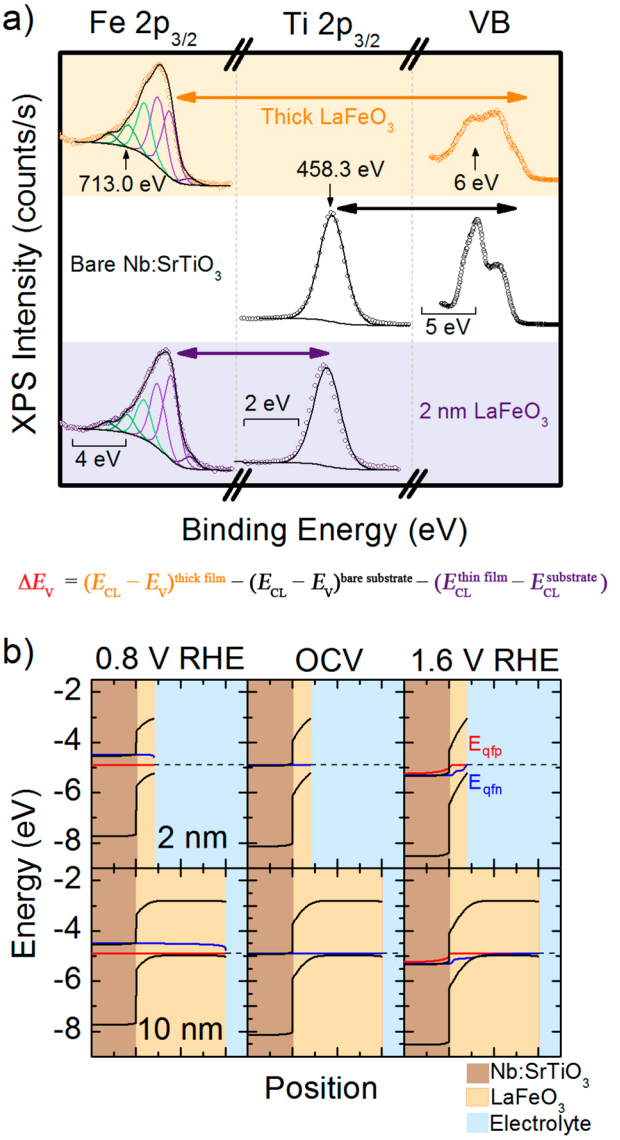

Figure 2. (a) XPS data for the 2 nm film, illustrating how the VBO is calculated. Intensity axes are not on a common scale any spectra. Energy axes are on a common scale (labeled) for a single atomic species' spectra for different samples, but not between different atomic species' spectra. Equation for VBO is shown below the XPS data for clarity. (b) Band diagrams calculated for the 2 and 10 nm films (top and bottom row) at 0.8 V, open-circuit voltage (OCV) of 1.2 V, and 1.6 V vs RHE (left to right), assuming a metallic contact at the surface junction at the redox level of $Fe(CN)_6^{4-}/Fe(CN)_6^{3-}$ and cathodic (anodic) potential forward (reverse) biases of the buried junction. Horizontal major scale ticks are 5 nm. The electron and hole quasi-Fermi levels (E_{qfn} and E_{qfh}) are shown for each condition. The dotted line represents the $Fe(CN)_6^{4-}/Fe(CN)_6^{3-}$ electrolyte redox level.

now be explained as a result of charge depletion throughout the film, with bands sloped upward toward the surface at all potentials, allowing photoexcited minority carrier electrons to be swept to the buried junction and into the Nb:$SrTiO_3$ substrate. This hypothesis is supported by the band calculations and valence band X-ray photoelectron spectroscopy, where the valence band was shown to be shifted further away from the Fermi level with decreasing film thickness (Figure S9c). The resulting valence band edge positions are approximately 100 mV below the electrolyte redox at 1.1 V vs RHE, with

DOI: 10.1021/acs.jpclett.5b00169
J. Phys. Chem. Lett. 2015, 6, 977−985

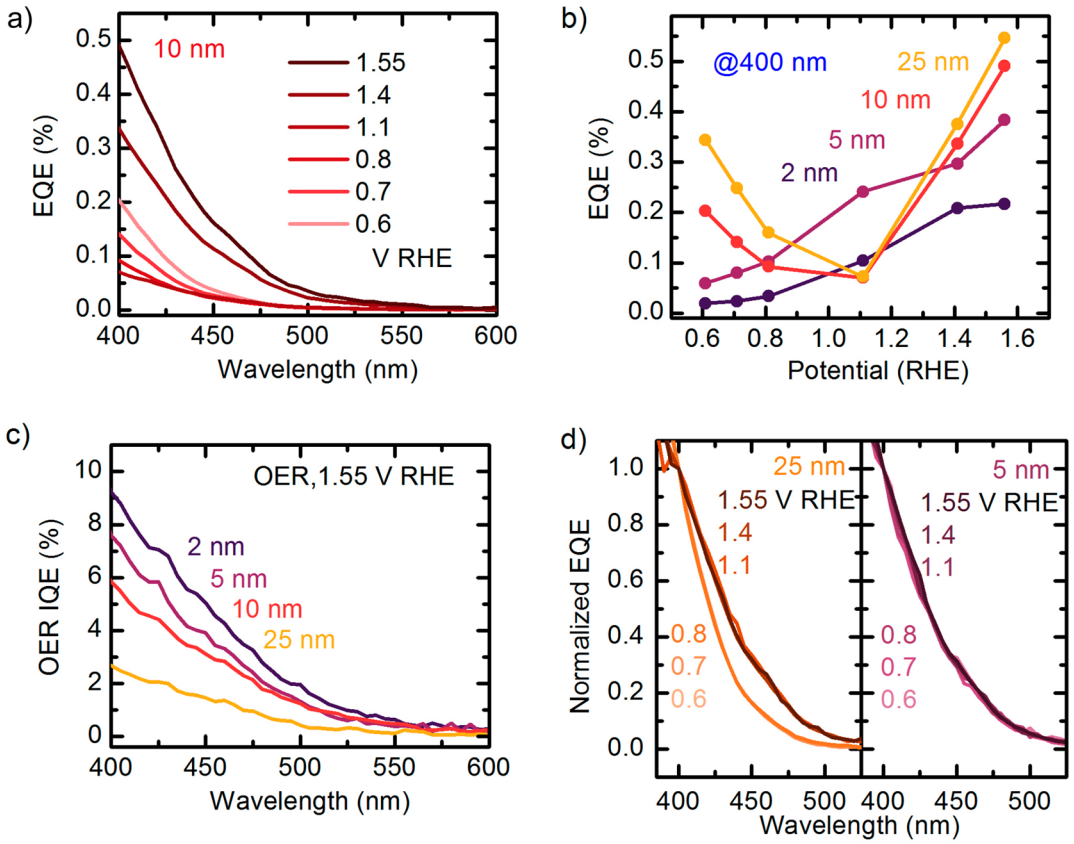

Figure 3. (a) The external quantum efficiency (EQE) of the 10 nm $LaFeO_3$ film is shown as a function of potential for incident wavelengths from 400 to 600 nm. (b) The EQE at 400 nm incident wavelength is shown as a function of potential for all film thicknesses. (c) The internal quantum efficiency (IQE) under oxygen evolution conditions (1.55 V RHE) is shown for each film thickness. (d) The EQE normalized to the value at a wavelength of 400 nm is shown for the 25 and 5 nm films at different applied potentials to illustrate the qualitative change in absorption at different applied potentials for thick and thin films.

corresponding vacuum energy of −4.9 eV, and are also in good agreement with the few Mott−Schottky estimates that are possible for the for the 10 and 25 nm films (1.0−1.1 V vs RHE, see Supporting Information and Figure S15).

The trade-off between increased absorption and reduced collection with increasing film thickness was examined by measuring photoelectrochemical external quantum efficiency (EQE) in 0.1 M KOH. The incident wavelength was varied from 400 to 600 nm, avoiding band-to-band absorption in the Nb:$SrTiO_3$ substrate while promoting it in the $LaFeO_3$. Figure 3a shows the wavelength- and potential-dependent EQE for the 10 nm film (corresponding plots for the 2, 5, and 25 nm films shown in Figure S12). The EQE was found to decrease smoothly with increasing wavelength and increase with increasing potential from OCV, where the highest EQE of ∼0.5% was noted for the most positive potential of 1.55 V RHE. At potentials more positive than OCV, the EQE increases because (1) the buried junction becomes increasingly reverse-biased, expanding the depletion layer in the $LaFeO_3$ film and increasing collection probability and (2) there is also additional overpotential driving the OER. EQE was found to increase with increasing film thickness at potentials more positive than OCV (Figure 3b), as expected from the increased absorption in a thicker film. When the potential is reduced toward the OCV, the depletion width narrows, which decreases the collection probability and the EQE. Since the electric field present in this depletion layer is responsible for sweeping excited minority carrier electrons across the buried junction, such potential-dependent depletion width changes should result in a potential-dependent quantum efficiency[10] as seen here.

The thinner films (2 and 5 nm) show monotonic improvement in EQE with increasing potential, while the thicker films (10 and 25 nm) show the smallest photoresponse near OCV, with EQE increasing as the absolute value of the potential increases (Figure S12). At potentials more negative than OCV (forward bias), the thicker films exhibit an increase in EQE from a typical *p*-type photoelectrochemical reduction current at the surface junction. As described above, the depletion region from the buried junction for thinner films is likely to extend across the entire film thickness, bending the bands upward toward the surface regardless of potential and reducing the probability that photogenerated electrons can diffuse across the surface junction to participate in a reduction reaction at the surface (Figure 2b), leading to a monotonic EQE response as a function of potential.

To further elucidate the thickness-dependent nature of the photocurrent in the $LaFeO_3$/Nb:$SrTiO_3$ devices, Figure 3c shows the *internal* quantum efficiency (IQE) for each film at 1.55 V RHE. To normalize the EQE data to IQE to account for only the photons actually absorbed within the $LaFeO_3$ active layer, a transfer matrix model was used to calculate the absorption in each film (Figure S13a) based on the complex index of refraction measured for each film by variable-angle spectroscopic ellipsometry measurements (Figures S4 and S5). Under OER conditions, IQE is highest for the thinner films ($IQE_{2\ nm} > IQE_{5\ nm} > IQE_{10\ nm} > IQE_{25\ nm}$, left axis), which is

DOI: 10.1021/acs.jpclett.5b00169
J. Phys. Chem. Lett. 2015, 6, 977−985

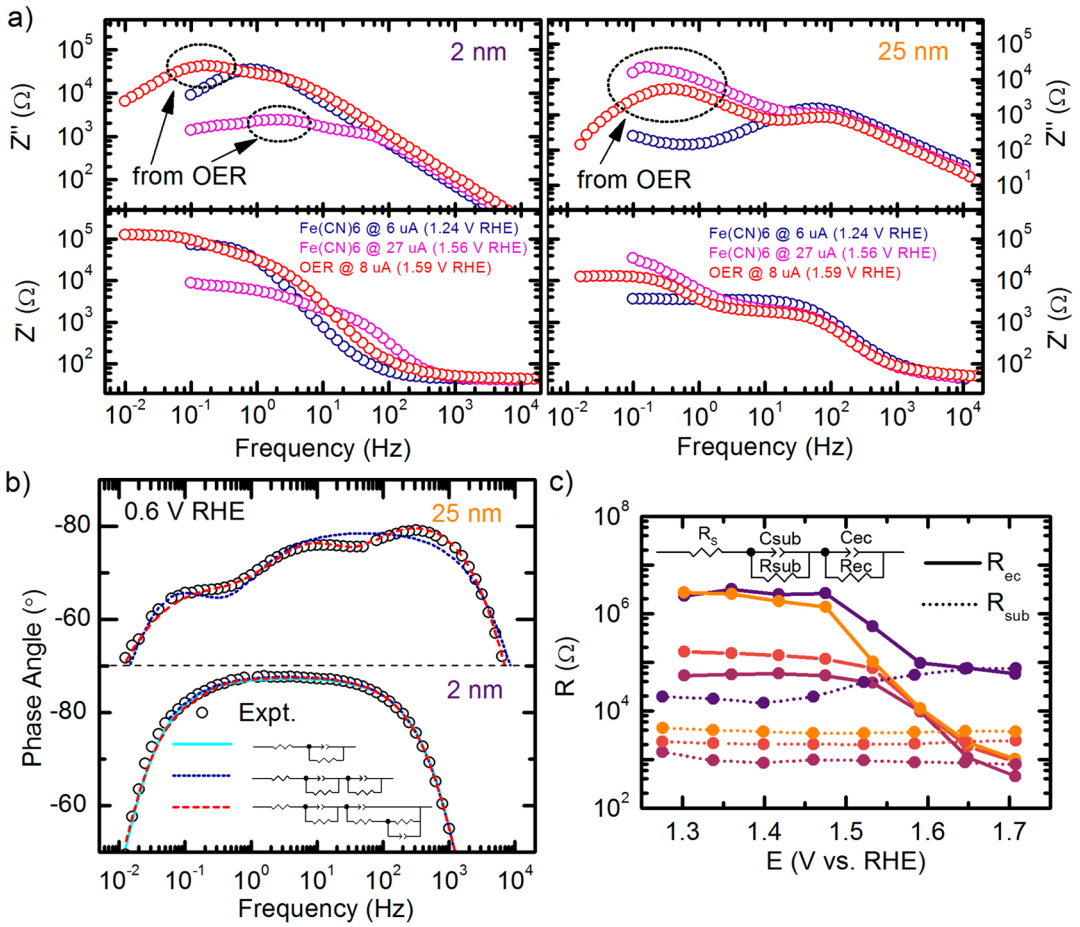

Figure 4. Electrochemical impedance spectroscopy (EIS): (a) comparison of impedance spectra of 2 nm (left) and 25 nm (right) $LaFeO_3$ in O_2-saturated 0.1 M KOH vs Ar-bubbled 0.1 M KOH + 0.01 M $Fe(CN)_6$, at similar current condition (~6−8 mA) and similar potential condition (~1.6 V RHE); (b) resistive circuit elements of the two-Randles circuit model from fitted EIS data vs applied potential in the OER range; and (c) EIS data of the 2 and 25 nm films in the ORR region (0.6 V RHE) in O_2-saturated 0.1 M KOH, where the film−substrate junctions are forward-biased.

consistent with the idea that the thinner films will be dominated by the depletion layer of the buried junction where the bands bend energetically upward closer to the surface, improving the IQE by increasing collection efficiency of oxidation current.

The wavelength dependence of the EQE (Figure 3d) provides support for the explanation of the OER current as minority carrier collection at the buried junction. Longer wavelength light is absorbed deeper in a given film, closer to the buried junction (Figure S13b). The slower decay of EQE with increasing wavelength under OER conditions for any given film in Figure 3d suggests that OER photocurrent is collected deeper in the film at the buried junction, with electrons swept away from the surface by significant band bending at anodic potentials. This potential-dependent profile is also visible in the IQE (Figure 3c).

Electrochemical impedance spectroscopy (EIS) was performed at a series of steady-state potential conditions to study the interaction between the multiple junctions of the films by the potential-dependent changes in capacitive elements (depletion regions). Measurements were taken in both KOH and $Fe(CN)_6$ electrolytes to ascertain if any frequency components are due to specific electrochemical reactions. Representative data collected from films of 25 and 2 nm are shown Figure 4a and 4b. The imaginary component of the impedance data collected from thick and thin films reveal one high-frequency (~100 Hz) and low-frequency (~0.1−1 Hz) process. The distinctive low-frequency feature was found only at higher applied potentials well above the equilibrium potential for OER for both the 25 and 2 nm films in both electrolytes (Figure 4a-b, and Figure S14). In contrast, at a similar current condition (giving a similar bias for the buried junction) only the $Fe[CN]_6$-free KOH electrolyte exhibits this feature. We therefore attribute this feature to surface-states at the surface junction, possibly from surface-oxygen intermediates of the OER.[51,52]

The high-frequency feature can be attributed to space-charge capacitances at both the buried junction and the surface junction, indicating the extent of the depletion regions in the film. With significant band bending and/or a completely depleted film (corresponding to OER potentials), the two junctions interact or overlap, and a single RC time constant will be distinguishable from EIS, aside from the OER surface states component. On the other hand, Figure 4c shows the 25 nm film EIS data at ORR conditions exhibiting three separate RC features (the two-Randles model is no longer qualitatively appropriate in this potential region) and can be fit by a circuit model with three RC time constants. When a quasi-neutral region in between the depletion regions is established in the thicker films due to decreased band bending at ORR potentials, the buried junction and surface junction depletion regions in the $LaFeO_3$ film are separated, allowing two RC time constants

DOI: 10.1021/acs.jpclett.5b00169
J. Phys. Chem. Lett. 2015, 6, 977−985

to be distinguished in EIS. The third RC feature is possibly surface states present during the ORR. The 2 nm film, however, can be fitted with a single RC time constant. There is little or no ORR activity with this film, so the single feature is attributed to what is effectively a single interface from the convolution of the substrate, depleted film, and electrolyte interfaces.

EIS data collected at potentials across the OER region were fit by a two-Randles circuit model (inset, Figure 4d). The circuit elements in Figure 4c indicate comparable buried junction resistances for the 5, 10, and 25 nm films as well as similar resistances for charge transfer to the electrolyte. These results are in good agreement with both the similar $Fe[CN]_6^{4-}$/$Fe[CN]_6^{3-}$ redox kinetics and the similar dark OER activity of these films (Figure 1). The 2 nm film, however, was found to have higher resistance in both of these elements. This higher resistance could be due to both a through-plane resistance effect and/or a change in the intrinsic dark OER activity of the surface. Further study is required to separate the true OER activity of the films uninfluenced by the buried junction, for example by a two-contact method.[53] For now, the EIS data indicate that the $LaFeO_3$ films show strongly potential-dependent device characteristics due to the varying interaction of the buried junction and surface junction and the development of a quasi-neutral region between the buried junction and surface junction at ORR potentials in thicker films, unlike the thinnest films which remain largely depleted at all potentials.

In this study, ultrathin $LaFeO_3$ films on $Nb:SrTiO_3$ have been shown to have strong potential- and thickness-dependent photoactivity for oxygen photoelectrocatalysis. Fast outer-shell redox electrochemistry revealed an increase in the through-plane charge transfer conductivity of the buried junction with thickness. Thicker films exhibited both photoelectrochemical ORR and OER activity, while thinner films exhibted only a photoelectrochemical OER response. EQE measurements and calculated band diagrams based on experimentally determined band alignment suggest this is a consequence of the changing width of the depletion regions and their extent into the film at different applied potentials, resulting in minority carriers being swept into either the substrate or the electrolyte. These findings are also supported by circuit models fitted to electrochemical impedance spectroscopy data. In the oft-proposed strategy of reducing oxide dimensions to allow improved carrier collection efficiency, bypassing the poor minority carrier lifetimes and diffusion lengths in most oxides, it becomes essential to understand in detail the properties of the interfaces present. This work emphasizes the importance of the interaction between bulk and interfacial material properties, where small changes in the thickness of a nanoscale oxide material can fundamentally change the nature of the interface between the film and the supportng substrate, with drastic effects on the charge transfer and carrier separation properties. This provides a possible path for improving buried-junction photoelectrochemical cells with active oxide layers, and may attract additional attention to using *p*-type oxides for water splitting. Understanding these types of material interactions at interfaces is necessary knowledge for the design of efficient oxide photoelectrodes.

EXPERIMENTAL METHODS

Thin Film Fabrication and Characterization. Pulsed laser deposition of the $LaFeO_3$ films was performed using a KrF excimer laser operating at 10 Hz and 1.5 J/cm^2. In the batch of films prepared, 1000, 2500, 5000, and 12500 pulses were used with the substrate at ∼645 °C under 200 mTorr O_2 to produce films of nominal thickess 2, 5, 10, and 25 nm, respectively. The $Nb:SrTiO_3$ substrates were (001)-oriented, 10 × 5 × 0.5 mm single crystal with 0.7 wt % Nb doping (MTI Corporation). The reflection high-energy electron diffraction (RHEED) pattern for the nominal 10 nm film is shown in Figure S1. Based on the observed oscillations, resulting film thicknesses were 1.8−2 nm ("2 nm"), 4.5−5 nm ("5 nm"), 8.9−10 nm ("10 nm"), and 22−25 nm ("25 nm"). Atomic force microscopy (AFM) and X-ray diffraction measurements confirm atomically flat surfaces with well-defined terraces corresponding to a slight substrate miscut, high crystallinity, and epitaxial alignment with the substrate growth (Figures S2 and S3, Supporting Information).

Voltammetry. Thin film samples were abraded on the back of the substrate and coated with Ga−In eutectic (99.99% purity, Sigma-Aldrich) before being electrically contacted with Ti wire, followed by silver paint (Ted Pella, Leitsilber 200) for adhesion, resulting in an ohmic contact (Figure S7). The samples were then coated with Omegabond 101 epoxy on the back surface, sides, and along the contacting wire to leave only the film surface (∼0.25 cm^2) exposed to electrolyte. Samples were lowered into a quartz electrochemical cell with Ag/AgCl reference electrode and a platinum wire counter electrode (all from Pine Instruments). The electrolyte was prepared with KOH pellets (99.99% purity, Sigma-Aldrich) and deionized water (>18 MΩ cm) to obtain a concentration of 0.1 M. For oxygen electrocatalysis measurements, oxygen (ultrahigh purity, Airgas) was bubbled for 20 min to ensure O_2/H_2O equilibrium at 1.23 V vs RHE, and bubbling continued during measurements. For $Fe(CN)_6$ experiments, 5 mM each of $K_4Fe(CN)_6 \cdot 3H_2O$ (99.99%, Sigma-Aldrich) and $K_3Fe(CN)_6$ (99%, Sigma-Aldrich) were added to the 0.1 M KOH solution after bubbling with argon (ultrahigh purity, Airgas) for 20 min (and continuing during experiments) to deoxygenate the electrolyte. The reference electrode was calibrated to RHE with a platinum working electrode in H_2-saturated (ultrahigh purity, Airgas) 0.1 M KOH electrolyte. Cyclic voltammetry was performed using a Biologic SP-300 potentiostat, with a scan rate of 10 mV s^{-1}. Sample illumination for photoelectrochemical measurements was obtained from a 150 mW 405 nm diode laser (OEM Laser Systems, Inc.) focused on the thin film to a spot size of ∼2−3 mm, which resulted in an incident beam power of ∼75 mW after attenuation from optical elements, as measured by a laser power meter (Ophir Nova II with Si sensor).

Quantum Efficiency. Light from a 300W Xe arc lamp was mechanically chopped at ∼8 Hz and coupled to a holographic grating monochromator for single-wavelength external quantum efficiency measurements (Newport Oriel). The photocurrent response as a function of bias was measured using an EG&G 263A potentiostat with current output coupled to a Merlin lock-in amplifier (Newport Oriel). To estimate the internal quantum efficiency, or absorbed photon conversion efficiency, the external quantum efficiency must be scaled appropriately to account for the fraction of light absorbed within the $LaFeO_3$ active layer. Because we have a 1D thin film system with planar interfaces, the transfer matrix method can be applied to model the propagation of light in the system.[54,55] A MATLAB code was used to calculate the transfer matrices using the *n* and *k* data fit for the $LaFeO_3$ films extracted from variable-angle spectroscopic ellipsometry measurements.[56] Due to additional reflection and scattering at the quartz/water

DOI: 10.1021/acs.jpclett.5b00169
J. Phys. Chem. Lett. 2015, 6, 977−985

interface in the photoelectrochemical setup the IQE measurements should have a relative accuracy of about ±10%.

Electrochemical Impedance Spectroscopy. Electrochemical impedance spectroscopy was performed in both O_2-saturated 0.1 M KOH and Ar-bubbled 0.1 M KOH with 0.01 M $Fe(CN)_6$. Data was acquired with a EG&G 263A potentiostat coupled with a Solartron 1260 impedance/gain-phase analyzer, with the exception of data taken in $Fe(CN)_6$ electrolyte, which was acquired with a Biologic SP-300. A single potential (∼1.6 V) was initially probed in the O_2-saturated solution. For comparison, spectra at both a similar applied potential and a similar current (which results in a comparable bias condition of the buried junction) were then collected in the $Fe(CN)_6$-containing electrolyte. A total of five integration cycles, with integration time of 0.2 s per cycle, were used for each data point. A single delay cycle was performed before acquiring data, after holding for 60 s at a potentiostatic condition. Experimental data is shown in Figure S6 in the Supporting Information. Data was analyzed with circuit fitting using ZView software (Scribner Associates).

X-ray Photoelectron Spectroscopy. X-ray photoelectron spectroscopy (XPS) spectra were collected on a Thermo Scientific K-Alpha XPS, using a dual beam source focused to a 400 μm spot size and ultralow energy electron beam for charge compensation. Binding energies were shifted to calibrate the energy scale to the adventitious carbon peak at 284.8 eV.[57,58] Details on the fitting procedure are available in the Supporting Information.

Band Diagrams. Band diagrams were generated using ADEPT 2.0, a web applet available on nanoHUB.org that solves the 1D Poisson equation simultaneously with the electron and hole continuity equations. Details on the simulation parameters are available in the Supporting Information.

■ ASSOCIATED CONTENT

Ⓢ Supporting Information

Further details on experimental methods, thin film growth, film and substrate characterization data (X-ray diffraction, reflective high-energy electron diffraction, spectroscopic ellipsometry, and X-ray photoelectron spectroscopy), optical modeling for internal quantum efficiency, band diagram simulations, and complete electrochemical impedance spectroscopy data are available free of charge via the Internet at http://pubs.acs.org.

■ AUTHOR INFORMATION

Corresponding Authors

*E-mail: kjmay@alum.mit.edu.
*E-mail: dfenning@eng.ucsd.edu.
*E-mail: shaohorn@mit.edu.

Present Address

⊥(D.L.) Center for Nanophase Materials Sciences, Oak Ridge National Laboratory, Oak Ridge, Tennessee 37831, United States.

Notes

The authors declare no competing financial interest.
#(M.D.B.) Author passed away Dec. 20, 2014.

■ ACKNOWLEDGMENTS

We thank Dr. Hans Christen for helpful comments and suggestions during the preparation of this manuscript. K.J.M. was supported in part by a doctoral postgraduate scholarship (PGS-D) from the Natural Sciences and Engineering Research Council of Canada (NSERC). D.P.F. acknowledges the support of the MIT/Battelle postdoctoral associate program. K.A.S. was supported by the National Science Foundation Graduate Research Fellowship under Grant No. DGE-1122374. This work was supported in part by the MRSEC Program of the National Science Foundation under Award No. DMR-0819762, and we thank the King Fahd University of Petroleum and Minerals in Dharam, Saudi Arabia, for funding the research reported in this paper through the Center for Clean Water and Clean Energy at MIT and KFUPM. This work was performed in part at Harvard University's Center for Nanoscale Systems (CNS), a member of the National Nanotechnology Infrastructure Network (NNIN), which is supported by the National Science Foundation under NSF Award No. ECS-0335765, and in part at the Center for Nanophase Materials Sciences, which is a DOE Office of Science User Facility. The authors dedicate this paper to the memory of Mike Biegalski, who will be remembered for his friendship and his tireless support.

■ REFERENCES

(1) Watanabe, T.; Fujishima, A.; Honda, K. Photoelectrochemical Reactions at $SrTiO_3$ Single Crystal Electrode. *Bull. Chem. Soc. Jpn.* **1976**, *49*, 355.

(2) Khaselev, O.; Turner, J. A. A Monolithic Photovoltaic-Photoelectrochemical Device for Hydrogen Production via Water Splitting. *Science* **1998**, *280*, 425.

(3) Walter, M. G.; Warren, E. L.; McKone, J. R.; Boettcher, S. W.; Mi, Q.; Santori, E. A.; Lewis, N. S. Solar Water Splitting Cells. *Chem. Rev.* **2010**, *110*, 6446.

(4) Gray, H. B. Powering the Planet with Solar Fuel. *Nat. Chem.* **2009**, *1*, 7.

(5) Morrish, R.; Rahman, M.; Macelroy, J. M. D.; Wolden, C. A. Activation of Hematite Nanorod Arrays for Photoelectrochemical Water Splitting. *ChemSusChem* **2011**, *4*, 474.

(6) Su, J.; Guo, L.; Bao, N.; Grimes, C. A. Nanostructured WO_3/$BiVO_4$ Heterojunction Films for Efficient Photoelectrochemical Water Splitting. *Nano Lett.* **2011**, *11*, 1928.

(7) Kronawitter, C. X.; Vayssieres, L.; Shen, S.; Guo, L.; Wheeler, D. A.; Zhang, J. Z.; Antoun, B. R.; Mao, S. S. A Perspective on Solar-Driven Water Splitting with All-Oxide Hetero-Nanostructures. *Energy Environ. Sci.* **2011**, *4*, 3889.

(8) Döscher, H.; Supplie, O.; May, M. M.; Sippel, P.; Heine, C.; Muñoz, A. G.; Eichberger, R.; Lewerenz, H.-J.; Hannappel, T. Epitaxial III−V Films and Surfaces for Photoelectrocatalysis. *ChemPhysChem* **2012**, *13*, 2899.

(9) Mills, T. J.; Lin, F.; Boettcher, S. W. Theory and Simulations of Electrocatalyst-Coated Semiconductor Electrodes for Solar Water Splitting. *Phys. Rev. Lett.* **2014**, *112*, 148304.

(10) Klahr, B. M.; Hamann, T. W. Voltage Dependent Photocurrent of Thin Film Hematite Electrodes. *Appl. Phys. Lett.* **2011**, *99*, 063508.

(11) Klahr, B. M.; Martinson, A. B. F.; Hamann, T. W. Photoelectrochemical Investigation of Ultrathin Film Iron Oxide Solar Cells Prepared by Atomic Layer Deposition. *Langmuir* **2011**, *27*, 461.

(12) Cox, C. R.; Winkler, M. T.; Pijpers, J. J. H.; Buonassisi, T.; Nocera, D. G. Interfaces Between Water Splitting Catalysts and Buried Silicon Junctions. *Energy Environ. Sci.* **2013**, *6*, 532.

(13) Stoerzinger, K. A.; Risch, M.; Suntivich, J.; Lü, W. M.; Zhou, J.; Biegalski, M. D.; Christen, H. M.; Venkatesan, T.; Shao-Horn, Y. Oxygen Electrocatalysis on (001)-Oriented Manganese Perovskite Films: Mn Valency and Charge Transfer at the Nanoscale. *Energy Environ. Sci.* **2013**, *6*, 1582.

(14) Arima, T.; Tokura, Y.; Torrance, J. B. Variation of Optical Gaps in Perovskite-Type 3d Transition-Metal Oxides. *Phys. Rev. B* **1993**, *48*, 15.

DOI: 10.1021/acs.jpclett.5b00169
J. Phys. Chem. Lett. 2015, 6, 977−985

(15) Scafetta, M. D.; Xie, Y. J.; Torres, M.; Spanier, J. E.; May, S. J. Optical Absorption in Epitaxial $La_{1-x}Sr_xFeO_3$ Thin Films. *Appl. Phys. Lett.* **2013**, *102*, 081904.
(16) Tijare, S. N.; Joshi, M. V.; Padole, P. S.; Mangrulkar, P. a.; Rayalu, S. S.; Labhsetwar, N. K. Photocatalytic Hydrogen Generation Through Water Splitting on Nano-Crystalline $LaFeO_3$ Perovskite. *Int. J. Hydrogen Energy* **2012**, *37*, 10451.
(17) Suntivich, J.; May, K. J.; Gasteiger, H. A.; Goodenough, J. B.; Shao-Horn, Y. A Perovskite Oxide Optimized for Oxygen Evolution Catalysis from Molecular Orbital Principles. *Science* **2011**, *334*, 1383.
(18) Li, S.; Jing, L.; Fu, W.; Yang, L.; Xin, B.; Fu, H. Photoinduced Charge Property of Nanosized Perovskite-Type $LaFeO_3$ and Its Relationships with Photocatalytic Activity under Visible Irradiation. *Mater. Res. Bull.* **2007**, *42*, 203.
(19) Parida, K. M.; Reddy, K. H.; Martha, S.; Das, D. P.; Biswal, N. Fabrication of Nanocrystalline $LaFeO_3$: An Efficient Sol−Gel Auto-Combustion Assisted Visible Light Responsive Photocatalyst for Water Decomposition. *Int. J. Hydrogen Energy* **2010**, *35*, 12161.
(20) Su, H.; Jing, L.; Shi, K.; Yao, C.; Fu, H. Synthesis of Large Surface Area $LaFeO_3$ Nanoparticles by SBA-16 Template Method as High Active Visible Photocatalysts. *J. Nanopart. Res.* **2010**, *12*, 967.
(21) Thirumalairajan, S.; Girija, K.; Hebalkar, N. Y.; Mangalaraj, D.; Viswanathan, C.; Ponpandian, N. Shape Evolution of Perovskite $LaFeO_3$ Nanostructures: A Systematic Investigation of Growth Mechanism, Properties and Morphology Dependent Photocatalytic Activities. *RSC Adv.* **2013**, *3*, 7549.
(22) Yang, J.; Zhong, H.; Li, M.; Zhang, L.; Zhang, Y. Markedly Enhancing the Visible-Light Photocatalytic Activity of $LaFeO_3$ by Post-Treatment in Molten Salt. *React. Kinet. Catal. Lett.* **2009**, *97*, 269.
(23) Yamamoto, A.; Sawa, A.; Akoh, H.; Kawasaki, M.; Tokura, Y. Electrical Properties of Oxide Heteroepitaxial p−n Junctions: $La_{1-x}Sr_xFeO_3/SrTi_{0.99}Nb_{0.01}O3$. *Appl. Phys. Lett.* **2007**, *90*, 112104.
(24) Sawa, A.; Yamamoto, A.; Yamada, H.; Fujii, T.; Kawasaki, M.; Matsuno, J.; Tokura, Y. Fermi Level Shift in $La_{1-x}Sr_xMO_3$ (M = Mn, Fe, Co, and Ni) Probed by Schottky-Like Heteroepitaxial Junctions with $SrTi_{0.99}Nb_{0.01}O_3$. *Appl. Phys. Lett.* **2007**, *90*, 252102.
(25) Yang, H.; Luo, H. M.; Wang, H.; Usov, I. O.; Suvorova, N. A.; Jain, M.; Feldmann, D. M.; Dowden, P. C.; DePaula, R. F.; Jia, Q. X. Rectifying Current-Voltage Characteristics of $BiFeO_3$/Nb-Doped $SrTiO_3$ Heterojunction. *Appl. Phys. Lett.* **2008**, *92*, 102113.
(26) Guo, S. M.; Zhao, Y. G.; Xiong, C. M.; Lang, P. L. Rectifying I−V Characteristic of $LiNbO_3$/Nb-Doped $SrTiO_3$ Heterojunction. *Appl. Phys. Lett.* **2006**, *89*, 223506.
(27) Zhang, P.; Gao, C.; Lv, F.; Wei, Y.; Dong, C.; Jia, C.; Liu, Q.; Xue, D. Hydrothermal Epitaxial Growth and Nonvolatile Bipolar Resistive Switching Behavior of $LaFeO_3$−$PbTiO_3$ Films on Nb:$SrTiO_3$(001) Substrate. *Appl. Phys. Lett.* **2014**, *105*, 152904.
(28) Watanabe, Y. Tunneling Current Through a Possible All-Perovskite Oxide p−n Junction. *Phys. Rev. B* **1998**, *57*, R5563.
(29) Cuellar, F. A.; Sanchez-Santolino, G.; Varela, M.; Clement, M.; Iborra, E.; Sefrioui, Z.; Santamaria, J.; Leon, C. Thermally Assisted Tunneling Transport in $La_{0.7}Ca_{0.3}MnO_3/SrTiO_3$:Nb Schottky-like Heterojunctions. *Phys. Rev. B* **2012**, *85*, 245122.
(30) Rossmeisl, J.; Qu, Z. W.; Zhu, H.; Kroes, G. J.; Nørskov, J. K. Electrolysis of Water on Oxide Surfaces. *J. Electroanal. Chem.* **2007**, *607*, 83.
(31) Reichman, J. The Current−Voltage Characteristics of Semiconductor-Electrolyte Junction Photovoltaic Cells. *Appl. Phys. Lett.* **1980**, *36*, 574.
(32) Rajeshwar, K. Fundamentals of Semiconductor Electrochemistry and Photoelectrochemistry. In *Encyclopedia of Electrochemistry: Semiconductor Electrodes and Photoelectrochemistry*; Bard, A. J., Stratmann, M., Licht, S., Eds.; Wiley-VCH: Weinheim, Germany, 2002; Vol. *6*, p 608.
(33) Albery, W. J. The Transport and Kinetics of Minority Carriers in Illuminated Semiconductor Electrodes. *J. Electrochem. Soc.* **1981**, *128*, 1492.
(34) Wilson, R. H. A Model for the Current−Voltage Curve of Photoexcited Semiconductor Electrodes. *J. Appl. Phys.* **1977**, *48*, 4292.
(35) Clarke, T. G.; Hampson, N. A.; Lee, J. B.; Morley, J. R.; Scanlon, B. Oxidations Involving Silver. I. Kinetics of the Anodic Oxidation of Silver in Alkaline Electrolytes. *Can. J. Chem.* **1968**, *46*, 3437.
(36) Muramatsu, T.; Muraoka, Y.; Hiroi, Z. Photocarrier Injection and Current−Voltage Characteristics of $La_{0.8}Sr_{0.2}MnO_3/SrTiO_3$:Nb Heterojunction at Low Temperature. *Jpn. J. Appl. Phys.* **2005**, *44*, 7367.
(37) Nakamura, M.; Sawa, A.; Fujioka, J.; Kawasaki, M.; Tokura, Y. Interface Band Profiles of Mott-Insulator/Nb:$SrTiO_3$ Heterojunctions as Investigated by Optical Spectroscopy. *Phys. Rev. B* **2010**, *82*, 201101.
(38) Fujioka, J.; Nakamura, M.; Kawasaki, M.; Tokura, Y. Photocarrier Collection from Depletion Layer of $LaMnO_3$. *J. Appl. Phys.* **2012**, *111*, 016107.
(39) Sawa, A.; Fujii, T.; Kawasaki, M.; Tokura, Y. Highly Rectifying $Pr_{0.7}Ca_{0.3}MnO_3/SrTi_{0.9998}Nb_{0.0002}O_3$ p−n junction. *Appl. Phys. Lett.* **2005**, *86*, 112508.
(40) Yang, K.; Kim, D. H.; Dho, J. Schottky Barrier Effect on the Electrical Properties of Fe_3O_4/ZnO and Fe_3O_4/Nb:$SrTiO_3$ heterostructures. *J. Phys. D Appl. Phys.* **2011**, *44*, 355301.
(41) Chambers, S. A.; Qiao, L.; Droubay, T. C.; Kaspar, T. C.; Arey, B. W.; Sushko, P. V. Band Alignment, Built-In Potential, and the Absence of Conductivity at the $LaCrO_3/SrTiO_3$(001) Heterojunction. *Phys. Rev. Lett.* **2011**, *107*, 206802.
(42) Kraut, E.; Grant, R.; Waldrop, J.; Kowalczyk, S. Precise Determination of the Valence-Band Edge in X-ray Photoemission Spectra: Application to Measurement of Semiconductor Interface Potentials. *Phys. Rev. Lett.* **1980**, *44*, 1620.
(43) Anderson, R. L. Germanium−Gallium Arsenide Heterojunctions. *IBM J. Res. Dev.* **1960**, *4*, 283.
(44) Robertson, J. Band Offsets of Wide-Band-Gap Oxides and Implications for Future Electronic Devices. *J. Vac. Sci. Technol., B* **2000**, *18*, 1785.
(45) Hong, W. T.; Stoerzinger, K. A.; Moritz, B.; Devereaux, T. P.; Yang, W.; Shao-Horn, Y. Probing $LaMO_3$ Metal and Oxygen Partial Density of States Using X-ray Emission, Absorption, and Photoelectron Spectroscopy. *J. Phys. Chem. C* **2015**, *119*, 2063.
(46) Klein, A. Energy Band Alignment at Interfaces of Semiconducting Oxides: A Review of Experimental Determination Using Photoelectron Spectroscopy and Comparison with Theoretical Predictions by the Electron Affinity Rule, Charge Neutrality Levels, and the Common Anion. *Thin Solid Films* **2012**, *520*, 3721.
(47) Kroemer, H. Problems in the Theory of Heterojunction Discontinuities. *CRC Crit. Rev. Solid State Mater. Sci.* **1975**, *5*, 555.
(48) Frensley, W.; Kroemer, H. Theory of the Energy-Band Lineup at an Abrupt Semiconductor Heterojunction. *Phys. Rev. B* **1977**, *16*, 2642.
(49) Unlu, H.; Nussbaum, A. A Review of Models for Heterojunction Band Offsets. *Solid-State Electron.* **1987**, *30*, 1095.
(50) Franciosi, A.; Van de Walle, C. G. Heterojunction Band Offset Engineering. *Surf. Sci. Rep.* **1996**, *25*, 1.
(51) Conway, B. E.; Liu, T. C. Characterization of Electrocatalysis in the Oxygen Evolution Reaction at Platinum by Evaluation of Behavior of Surface Intermediate States at the Oxide Film. *Langmuir* **1990**, *6*, 268.
(52) Klahr, B.; Gimenez, S.; Fabregat-Santiago, F.; Hamann, T.; Bisquert, J. Water Oxidation at Hematite Photoelectrodes: The Role of Surface States. *J. Am. Chem. Soc.* **2012**, *134*, 4294.
(53) Lin, F.; Boettcher, S. W. Adaptive Semiconductor/Electrocatalyst Junctions in Water-Splitting Photoanodes. *Nat. Mater.* **2013**, *13*, 81.
(54) Pettersson, L. A. A.; Roman, L. S.; Inganäs, O. Modeling Photocurrent Action Spectra of Photovoltaic Devices Based on Organic Thin Films. *J. Appl. Phys.* **1999**, *86*, 487.
(55) Peumans, P.; Yakimov, A.; Forrest, S. R. Small Molecular Weight Organic Thin-Film Photodetectors and Solar Cells. *J. Appl. Phys.* **2003**, *93*, 3693.
(56) Burkhard, G. F.; Hoke, E. T.; McGehee, M. D. Accounting for Interference, Scattering, and Electrode Absorption to Make Accurate

DOI: 10.1021/acs.jpclett.5b00169
J. Phys. Chem. Lett. 2015, 6, 977−985

Internal Quantum Efficiency Measurements in Organic and Other Thin Solar Cells. *Adv. Mater.* **2010**, *22*, 3293.
(57) Barr, T. L. Nature of the Use of Adventitious Carbon as a Binding Energy Standard. *J. Vac. Sci. Technol., A* **1995**, *13*, 1239.
(58) Swift, P. Adventitious Carbon—The Panacea for Energy Referencing? *Surf. Interface Anal.* **1982**, *4*, 47.

DOI: 10.1021/acs.jpclett.5b00169
J. Phys. Chem. Lett. 2015, 6, 977−985